Microporous and Mesoporous Materials 296 (2020) 109994

Contents lists available at ScienceDirect

Microporous and Mesoporous Materials

journal homepage: http://www.elsevier.com/locate/micromeso

Dynamic benzene adsorption performance of microporous TMA^+-exchanged montmorillonite: The role of TMA^+ cations

Liangliang Deng [a,b], Yaqi Liu [a,b], Guanzheng Zhuang [a,b], Peng Yuan [a,b,*], Dong Liu [a,b], Hongling Bu [a,b], Hongzhe Song [a,b], Li Li [a,b]

[a] CAS Key Laboratory of Mineralogy and Metallogeny / Guangdong Provincial Key Laboratory of Mineral Physics and Materials, Guangzhou Institute of Geochemistry, Institutions of Earth Science, Chinese Academy of Sciences, Guangzhou, 510640, China
[b] University of Chinese Academy of Sciences, Beijing, 100049, China

ARTICLE INFO

Keywords:
Montmorillonite
TMA^+ exchanging
Surfactant dosage
Micropores
Dynamic adsorption
Benzene

ABSTRACT

Tetramethylammonium (TMA^+) exchanged montmorillonites (TMA-Mts) of various surfactant (TMA^+) dosages were prepared, and the roles of TMA^+ cations in the microstructure and dynamic benzene adsorption performance of TMA-Mts were investigated. TMA^+ cations were intercalated into the interlayer space of montmorillonite (Mt), and they exhibited dual effects on the benzene adsorption by TMA-Mts. For one thing, the intercalated TMA^+ cations arranged loosely, creating an interlayer microporous structure. The interlayer micropores were important benzene adsorption sites, and the dynamic benzene adsorption capacity (q value) positively correlated to the microporous surface area (S_{micro}). The optimized dosage of TMA^+ was 1.5 times the cation exchange capacity of Mt itself, which resulted in a TMA-Mt with the largest S_{micro} and q values of 65.0 m^2/g and 425.3 mg/g, respectively. On the other hand, the intercalated TMA^+ cations could interact with benzene molecules, further increasing the benzene adsorption performance of TMA-Mt but decreasing the diffusion and mass transfer of benzene molecules through TMA-Mt. In addition, TMA-Mt displayed remarkable regenerability, with a recycling efficiency exceeding 90%. These results indicated that modifying montmorillonite with small quaternary ammonium cation is an effective strategy to enhance the adsorption of volatile organic compounds (VOCs) by Mt and the TMA-Mts are promising adsorbents for VOCs remediation.

1. Introduction

Volatile organic compounds (VOCs), which emitted from the construction, petrochemical, pharmaceutical, and printing industries, are the most common air pollutants, and they are toxic and (in some cases) carcinogenic [1]. In addition, VOCs are the primary contributors to photochemical pollution and secondary organic aerosols, which are also harmful to human health [2–4]. Therefore, the treatment of VOCs had received considerable attention. Many technologies have been developed for VOCs control, such as membrane separation [5], oxidation [6], catalysis [7], biological treatment [8], and adsorption [9], where absorption is the most applicable technology because of its low cost, low energy, and flexible system structure [10].

Adsorbents play an important role in the application of adsorption technology, and activated carbon and synthetic zeolites are two types of commonly used VOCs adsorbents. Activated carbon is inexpensive and exhibits excellent adsorption capacity [11], but several drawbacks are associated with its use in the adsorption process, such as fire risk, propensity for pore-clogging, and regeneration difficulties [12]. Synthetic zeolites, such as ZSM-5 [13] and NaY zeolites [14], have the advantages in VOCs adsorption due to their good chemical stability and controllable pore size, but their wide application is restricted by their high cost. There is therefore an increasing focus on the development of low-cost adsorbents with excellent adsorption performance and desirable thermal stability. To this end, raw minerals have been proposed as possible adsorbents due to their unique porous structure, excellent heat resistance, and low cost [15].

Montmorillonite (Mt) is a 2:1 dioctahedral clay mineral comprising an octahedral alumina sheet sandwiched between two opposing tetrahedral silica sheets, with hydrated exchangeable cations incorporated within the interlayer space. In addition, the substitution of Mg^{2+} or Fe^{2+} for Al^{3+} in octahedral sheets and substitution of Al^{3+} for Si^{4+} in

* Corresponding author. CAS Key Laboratory of Mineralogy and Metallogeny, Guangzhou Institute of Geochemistry, Institutions of Earth Science, Chinese Academy of Sciences, Wushan, Guangzhou, 510640, China.
E-mail address: yuanpeng@gig.ac.cn (P. Yuan).

https://doi.org/10.1016/j.micromeso.2019.109994
Received 31 August 2019; Received in revised form 19 December 2019; Accepted 28 December 2019
Available online 30 December 2019
1387-1811/

tetrahedral sheets often occurs in Mt, making the layers of Mt negatively charged. Due to the exchangeable cations and negatively charged layers, Mt is widely used as an efficient adsorbent for the removal of aqueous cationic pollutants, such as dyes [16] and heavy metal ions [17], from wastewaters. However, the adsorption of Mt for non-ionic organic pollutants (NOPs), e.g., benzene [18] and phenol [19], is hindered by its hydrophilicity, which results from the exchangeable cations and negatively charged layers. The modification of Mt via a cation-exchange reaction with cationic surfactants, such as octadecyltrimethylammonium bromide (OTAB) [20], cetyltrimethylammonium bromide (CTAB) [21], dodecyltrimethylammonium bromide (DTAB) [22], and tetramethylammonium bromide (TMAB) [23], forms organo-montmorillonites (OMts). The cationic surfactants are intercalated within the interlayer spaces of Mt, leading to different overall physical and chemical properties for OMts, including a NOPs absorptive capacity superior to that of Mt [24].

In physical terms, the intercalated surfactants convert the OMts surface from hydrophilic to hydrophobic [25], and thus improve its affinity for hydrophobic NOPs. Moreover, the intercalated surfactants affect the microstructure of OMts, resulting in various NOPs adsorption behaviors. Two adsorption mechanisms have been reported: (1) a partition process, and (2) a surface-adsorbent process [26,27]. Previous studies have revealed that the intercalation of large surfactants (e.g., CTAB and DTAB, as mentioned above) in the interlayer space of Mt occurs via close packing to form hydrophobic phase, which were considered to adsorb NOPs by a partition process [28]. Conversely, OMts modified with small surfactants (e.g., TMAB) usually adsorb organic pollutants via a surface-adsorbent process, because small surfactant molecules tend to be loosely arranged in the interlayer space, creating a number of micropores [29].

Compared with the numerous studies of NOPs adsorption by OMts, the report on the VOCs adsorption by OMts was rare, and the relevant mechanisms were still unclear. Generally, an adsorbent with a large specific surface area (S_{BET}) and many micropores will exhibit excellent VOCs adsorption performance [30]. The OMts modified with small surfactants (e.g., TMAB) has a larger S_{BET} value and more interlayer micropores than those OMts containing larger surfactants [29], and may thus possess excellent VOCs adsorption performance. However, several factors, such as surfactant size and charge density of Mt, influenced the microstructure of OMts modified with small surfactants, and would thus have an impact on the VOCs adsorption. Kukkadapu et al. [31] found that the organic-vapor adsorption performance of OMts comprising small surfactants of different size (TMAB and tetramethylphosphonium bromide) depended on their S_{BET} values, i.e., a larger value of S_{BET} corresponded to a greater adsorption capability. Lee et al. [32] reported that the charge density of Mt influenced the VOCs adsorption behavior of TMA-Mt by affecting the packing density of TMA^+ cations and the formation of micropores.

However, the adsorption behavior of OMts incorporating small surfactants is not only regulated by surfactant size and charge density of Mt, but also affected by surfactant dosage, which controls the microstructure of the resulting OMts [29]. Surprisingly, the role of TMA^+ cations on the VOCs adsorption performance of TMA-Mts with different TMA^+ dosages has not been reported.

In addition, in previous research, VOCs adsorption by TMA-Mts was evaluated using static adsorption experiment [31,32], whose processes include the pre-evacuating of adsorbents and the altering of adsorption and desorption equilibrium pressures [33]. In comparison, dynamic adsorption experiment conducted at room temperature and atmospheric pressure can be used to simulate the real adsorption behavior of adsorbents for industrial VOCs-absorbing applications. Hence, studying the dynamic adsorption of VOCs by TMA-Mts is necessary for further applications of this technique.

To examine these two areas, the microstructure of TMA-Mts prepared with various TMA^+ dosages were characterized. Benzene, one of the most common VOCs pollutants, was used to investigate the dynamic adsorption behavior of TMA-Mts. Finally, the role of TMA^+ cations on the dynamic benzene adsorption performance of TMA-Mts was examined and discussed.

2. Experiment

2.1. Materials

Mt sourced from Inner Mongolia, China, was purified by a conventional sedimentation method, and its chemical composition was as follows: SiO_2, 57.41%; Al_2O_3, 15.66%; Fe_2O_3, 4.93%; MgO, 4.98%; K_2O, 0.12%; CaO, 2.98%; Na_2O, 0.11%; MnO, 0.03%; TiO_2, 0.31%; and ignition loss, 13.33%. The cation-exchange capacity (CEC) of purified Mt, measured by adsorption of $[Co(NH_3)_6]^{3+}$ [34], was 110.5 meq/100 g. TMAB (>98%) was purchased from Sigma-Aldrich Chemistry Co., Ltd.

2.2. Preparation of TMA-Mt

Sodium-based montmorillonite (Na–Mt) was firstly prepared as follows: 10.0 g purified Mt was dispersed in 200 mL of a 0.5 M sodium chloride solution under vigorous stirring at 80 °C for 24 h. After this time, the solid phase was then separated from the solution by centrifugation and then re-treated with 200 mL of 0.5 M sodium chloride solution, and the resulting mixture was heated and then separated as before. This procedure was repeated once more to effect complete cation exchange. The Na–Mt product was repeatedly washed with distilled water and then dried at 60 °C overnight before it was ground to a powder.

TMA-Mt was prepared by the following method: a desired amount of TMAB, equating to several times (0.25, 0.5, 1.0, 1.5, and 2.0, respectively) of the CEC of the amount of Na–Mt, was dispersed in 200 mL of distilled water, and the solution was stirred at 80 °C for 30 min. Then, 10.0 g Na–Mt was added slowly into the solution, and the mixture was stirred at 60 °C for 12 h. After this time, the solids were separated by filtration, repeatedly washed with distilled water to remove excess TMAB, and then dried and ground. The products are denoted as TMA-Mtx, where x was the dosage of TMAB. For example, $TMA\text{-}Mt_{0.25}$ denotes TMA-Mt with a TMAB dosage of 0.25 CEC.

2.3. Characterization methods

Major element oxides were analyzed on fused glass beads with a Rigaku RIX 2000 X-ray fluorescence spectrometer. To determine loss on ignition, 1000 mg of sample powder was heated to 1000 °C and maintained there for 10 min.

The CHN elemental analysis was performed using an ElementarVario EL III Universal CHNOS Elemental Analyzer.

The thermogravimetric (TG) analysis was conducted on a Netzsch STA 409 PC instrument. Approximately 10 mg of the sample was heated in a corundum crucible from 30 to 1000 °C at a heating rate of 10 °C/min under a highly pure N_2 atmosphere (20 cm^3/min).

The X-ray diffraction (XRD) patterns were recorded with a Bruker D8 Advance diffractometer with a Ni filter and Cu-Kα radiation ($\lambda = 0.154$ nm) using a generator voltage of 40 kV and a current of 40 mA. The scan rate was 3° (2θ)/min.

Ar adsorption-desorption isotherms were measured with a Micromeritics ASAP-2460 Accelerated Surface Area and Porosimetry system at liquid-argon temperature. The samples were outgassed at 120 °C for 12 h before measurements were made. The samples' S_{BET} values were calculated from the argon adsorption data using the multiple-point Brunauer-Emmett-Teller (BET) method [35], and the total pore volume (V_{total}) was estimated based on the argon uptake at a relative pressure of approximately 0.98. The samples' microporous surface area (S_{micro}) and microporous volume (V_{micro}) were derived using the *t*-plot method [36]. The non-local density functional theory (NLDFT) model [37] was used to determine the samples' micropore size distributions.

Diffuse reflectance infrared Fourier-transform (DRIFT) characterization was performed on the Praying Mantis™ diffuse reflection accessory (Harrick Scientific Products INC) of a Bruker Vertex-70 Fourier transform infrared spectrometer at room temperature. The DRIFT measurement lasted for 2 min (from the sample loading to the spectrum recording), and the ambient relative humidity was approximately 30%. The spectra were collected over the range of 600–4000 cm^{-1} with 64 scans and a resolution of 4 cm^{-1} using a KBr background.

2.4. Benzene adsorption test

The samples' benzene adsorption performance was evaluated with an in-line gas chromatography apparatus (Fig. 1). Before adsorption, the samples were heated at 120 °C in a muffle oven for 2 h to remove most of the physically adsorbed water molecules and small organic impurities adsorbed in the pores. During the adsorption measurement, an organic saturator containing 200 mL benzene was immersed in a water bath at 30 °C. Each powder sample was weighed accurately to 0.5 g and loaded into a glass column. The column was fed with a dry nitrogen stream containing benzene vapor at 3.00 mL/min, which was adjusted as required with a mass flow controller (MFC). The concentrations of benzene in both the column influent and effluent were quantified with a gas chromatograph (Agilent 7820A) using flame ionization detection. The experiment stopped when the adsorption equilibrium for the adsorbent was reached. After adsorption, the glass column containing the sample was heated at 120 °C for 12 h for desorption of the adsorbed benzene molecules, cooled to room temperature, and retested. This adsorption-desorption cycle test was performed four times to evaluate the samples' regenerative and re-use performance.

The adsorbents' benzene adsorption capacity (q, mg/g) was calculated by integrating the area above the acquired breakthrough curve after subtracting the area attributable to dead volume in the system, according to the following equation:

$$q = \frac{M}{1000m}\int_{t_1}^{t_2} F[C_0 - C_t]dt \qquad \text{Eq. (1)}$$

where M (g/mol) is the molecular mass of benzene; m (g) is the initial mass of the adsorbents before testing; t_1 (min) is the breakthrough time without the samples; t_2 (min) is the breakthrough time with the packed column; C_0 and C_t (mmol/L) represent the influent and measured effluent benzene concentrations, respectively; and F (mL/min) is the N_2 flow rate. The dead volume was determined by performing blank runs without the column.

The breakthrough curves were fitted using the Yoon and Nelson model [38], as per Eq (2):

$$t = \tau + \frac{1}{k}\ln\frac{C_t}{C_0 - C_t} \qquad \text{Eq. (2)}$$

where t (min) is the breakthrough time; C_t and C_0 are the outlet and inlet concentrations of the stream through the adsorbent column, respectively; τ (min) is the time at which the breakthrough concentration reached half the initial concentration ($C_t = 0.5\ C_0$); and k is the mass transfer coefficient.

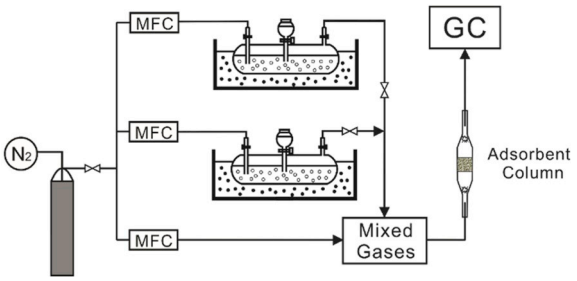

Fig. 1. Schematic diagram of experimental set-up.

3. Results and discussion

3.1. Microstructure of TMA-Mtx samples

The XRD patterns of Na–Mt and TMA-Mtx samples are presented in Fig. 2. The (001) reflection of Na–Mt occurs at 7.2° (2θ), corresponding to a d_{001}-value of 1.26 nm. A weak reflection at 27° is attributed to quartz (ca. wt. 3%). Compared to Na–Mt, the d_{001}-values of TMA-Mtx samples increased to 1.31 nm (TMA-$Mt_{0.25}$) and 1.38 nm (TMA-$Mt_{0.5}$, TMA-$Mt_{1.0}$, TMA-$Mt_{1.5}$, and TMA-$Mt_{2.0}$), corresponding to interlayer distances of 0.35 nm and 0.42 nm. These were calculated by subtracting the thickness of the structural TOT layer unit (0.96 nm) from d_{001}-value. The increase of the basal spacing demonstrates the successful intercalation of TMA^+ cations, in accordance with previous study [23]. The basal spacing of TMA-Mtx samples was positively influenced by surfactant (TMA^+) dosage. However, TMA^+ dosage of more than 0.5 CEC resulted in the same basal spacing. This phenomenon indicates that the basal spacing of TMA-Mtx samples is limited.

The carbon (f_C) and nitrogen (f_N) content of Na–Mt and TMA-Mtx samples are listed in Table 1. The f_C and f_N of TMA-Mtx samples were larger than those of Na–Mt and enlarged with the increase of TMA^+ dosage. These results were ascribed to the increase in the amount of intercalated TMA^+ cations. The Δf_C and Δf_N values (Table 1) dramatically increased until the TMA^+ dosage reached 1.0 CEC while more TMA^+ resulted in only a little increase of Δf_C and Δf_N values. This phenomenon suggests that the TMA^+ dosage of 1.0 CEC is a critical point which indicates different intercalation mechanisms [39]. TMA^+ cations intercalated into the interlayer space of Na–Mt mainly by ion-exchanging when TMA^+ dosage is less than 1.0 CEC, while TMA^+ cations can be also physically adsorbed into the interlayer space and/or surface of Na–Mt via ion pairs when they are more than 1.0 CEC. However, only a few TMA^+ cations can occupy the interlayer space and surface by physical adsorption.

TG/DTG measurement was performed to calculate the content of TMA^+ in TMA-Mtx samples. The TG curve of Na–Mt (Fig. 3a) showed two mass loss steps in the temperature range of 30–200 °C and 500–700 °C with the related DTG peaks centered at 115.7 and 626.6 °C, respectively. The former substantial loss was attributed to the dehydration of adsorbed water and interlayer water, indicating a water content of 10.03%. While, the latter mass loss occurred at a temperature of higher than 500 °C was caused by the dehydroxylation of Na-Mt [40]. Three

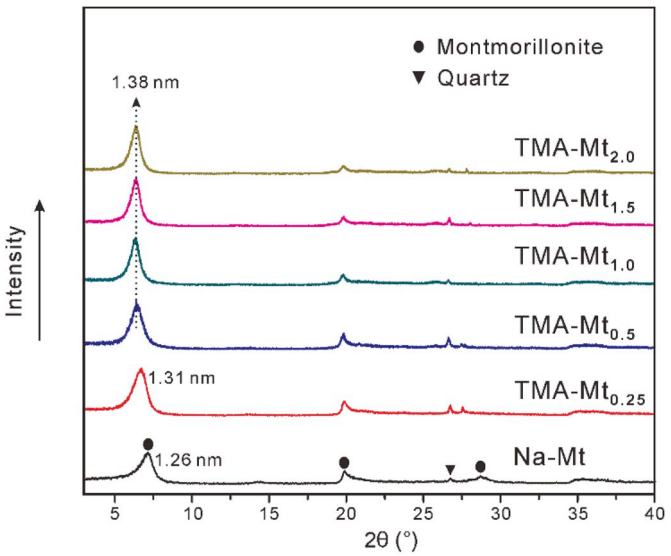

Fig. 2. XRD patterns of Na–Mt and TMA-Mtx samples.

Table 1
Total carbon (f_C) and nitrogen (f_N) content of Na–Mt and TMA-Mtx samples.

Samples	f_C (by mass, %)	Δf_C	f_N (by mass, %)	Δf_N
Na–Mt	0.074	0.000	0.044	0.000
TMA-$Mt_{0.25}$	1.720	1.646	0.380	0.336
TMA-$Mt_{0.5}$	2.700	2.626	0.720	0.676
TMA-$Mt_{1.0}$	4.270	4.196	1.100	1.056
TMA-$Mt_{1.5}$	4.600	4.526	1.160	1.116
TMA-$Mt_{2.0}$	4.750	4.676	1.240	1.196

Note: $\Delta f_C = f_C$ (TMA-Mt) - f_C (Na–Mt), $\Delta f_N = f_N$ (TMA-Mt) – f_N (Na–Mt).

major mass loss steps centered at 113.2, 397.5, and 585.7 °C are resolved in the TG curve of TMA-$Mt_{0.25}$ (Fig. 3b): (1) the removal of adsorbed water and interlayer water at 30–200 °C, (2) the decomposition of the intercalated TMA^+ in the temperature range of 200–500 °C, and (3) the dehydroxylation at the temperature above 500 °C. Compared to Na–Mt, the water content of TMA-$Mt_{0.25}$ decreased to 9.13%. This result was due to improvement of the hydrophobicity of Na–Mt by the intercalation of TMA^+ cations with a content of 4.22%. With the increase of the TMA^+ dosage, the water content of TMA-$Mt_{0.5}$, TMA-$Mt_{1.0}$, TMA-$Mt_{1.5}$, and TMA-$Mt_{2.0}$ (Fig. 3c–f) further decreased to 8.43%, 7.36%, 6.59%, and 5.80%, respectively, but their content of intercalated TMA^+ cations increased to 5.83%, 8.68%, 9.52%, and 10.11%, respectively. These results confirmed the enhancement of hydrophobicity of TMA-Mtx samples by the intercalation of TMA^+ cations.

The Ar adsorption-desorption isotherms of Na–Mt and TMA-Mtx samples are displayed in Fig. 4a. According to the IUPAC classification refined by Thommes et al. [37], the isotherm of Na–Mt was classified as type II with an H3 hysteresis loop, which is a characteristic of plate materials with non-rigid slit-like pores [41]. Hysteresis is associated with the filling and emptying of mesopores via capillary condensation,

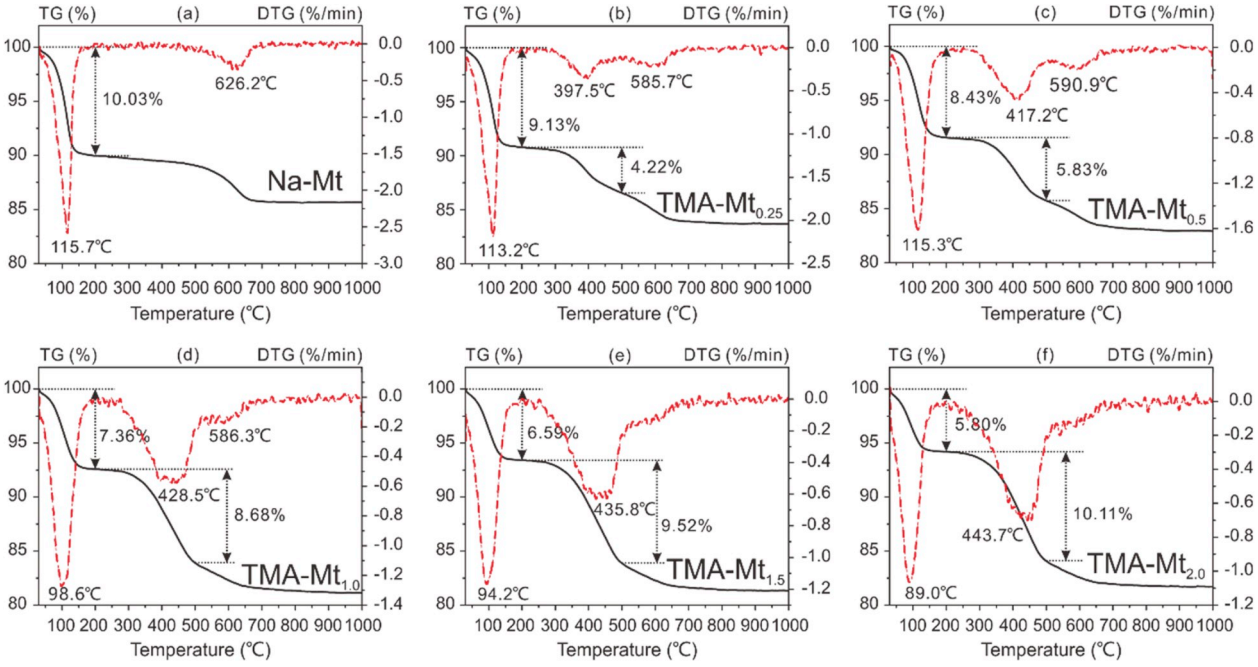

Fig. 3. TG and DTG curves of (a) Na–Mt, (b) TMA-$Mt_{0.25}$, (c) TMA-$Mt_{0.5}$, (d) TMA-$Mt_{1.0}$, (e) TMA-$Mt_{1.5}$, and (f) TMA-$Mt_{2.0}$.

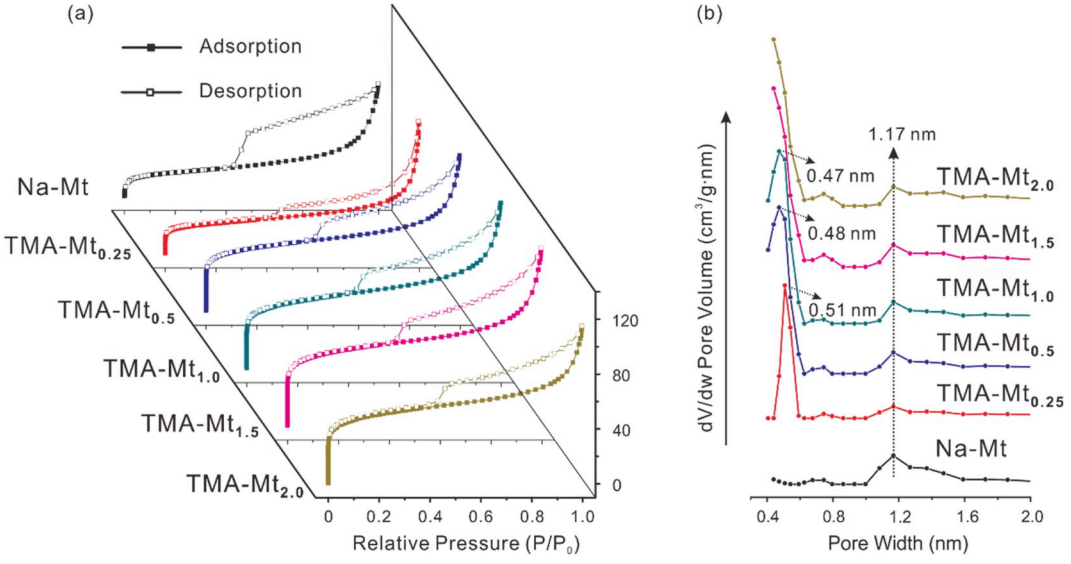

Fig. 4. Ar adsorption-desorption isotherms (a) and NLDFT pore size distribution (PSD) curves (b) of Na–Mt and TMA-Mtx samples.

where these mesopores result from the disordered stacking of Na–Mt particles. A slightly steeper increase in adsorption at a low relative pressure ($P/P_0 < 0.1$) in the isotherm of Na–Mt (Fig. 4a) indicated the presence of micropores in this substrate. These micropores corresponded to the slit-shaped micropores created by the turbostratic stacking of clay particles and/or the interlayer micropores resulting from dehydration [15].

The isotherms of TMA-Mtx samples (Fig. 4a) present mixed characteristics of type I(a) and IV(a) with an H3 hysteresis loop, which indicated the coexistence of microporosity and mesoporosity. The hysteresis loop was caused by mesopores formed by disordered stacking of particles. Moreover, the amount of adsorbed Ar at relatively low pressure ($P/P_0 < 0.1$) in the isotherms of TMA-Mtx samples increased much more rapidly than that amount adsorbed in Na–Mt, suggesting that TMA-Mtx samples had a more highly developed microporosity than Na–Mt. This can be attributed to the intercalated TMA^+ cations, which created a number of micropores in the interlayer of TMA-Mtx samples.

The micropore size distribution (PSD) curves of Na–Mt and TMA-Mtx samples (Fig. 4b) showed a minor distribution at 1.17 nm, which is much greater than the interlayer distance of Na–Mt and TMA-Mx samples. Hence, these micropores probably resulted from the turbostratic stacking of particle. In addition, a remarkable distribution centered at 0.51 nm appeared in the PSD curves of TMA-$Mt_{0.25}$. With the increase of TMA^+ dosage, the diameters of these micropores decreased in TMA-$Mt_{0.5}$ (0.48 nm) and TMA-$Mt_{1.0}$ (0.47 nm), and finally decreased to lower than the detection limit in TMA-$Mt_{1.5}$ and TMA-$Mt_{2.0}$. Hence, these micropores were attributed to the unevenly occupation of TMA^+ cations in the interlayer space. The increase of the density of intercalated TMA^+ cations leads to close packing from loose distribution, resulting in the decrease of micropore size.

The porous parameters of the Na–Mt and TMA-Mtx samples are listed in Table 2. Na–Mt showed the smallest S_{BET} (55.9 m^2/g) due to its poorest microporosity, of which the S_{micro} was only 3.3 m^2/g. This result was in accordance with the slight phenomenon of micropore filling in the Ar adsorption-desorption isotherms of Na–Mt (Fig. 4a). After TMA^+ exchanging, the S_{BET} and S_{micro} of TMA-Mtx samples increased, owing to the formation of the interlayer micropores by the intercalation of TMA^+ cations. TMA-$Mt_{1.5}$ had the highest S_{BET} and S_{micro} (173.5 m^2/g and 65.0 m^2/g, respectively), indicating that a dosage of 1.5 CEC is considered the critical point. When the TMA^+ dosage outstripped 1.5 CEC, the exceeded TMA^+ cations could also be intercalated into the interlayer space of Na–Mt by adsorption, resulting in the decrease of the interlayer microporosity of TMA-Mtx samples.

3.2. Dynamic benzene adsorption of TMA-Mtx samples

The breakthrough curves of Na–Mt and TMA-Mtx samples (Fig. 5) were used to evaluate their dynamic adsorption capacity (q value, Table 3). Na–Mt had the lowest q value (87.1 mg/g), attributing to its smallest S_{BET} and least amount of micropores. In addition, as the XRD patterns (Fig. 2) indicated, the interlayer distance of Na–Mt was only approximately 0.30 nm, which was less than the van der Waals diameter of the carbon atom (0.34 nm), the smallest one-dimensional size that a benzene molecule could adopt. Therefore, only a small number of the interlayer micropores of Na–Mt (i.e. the micropores with the pore width

Table 2
Porous parameters of Na–Mt and TMA-Mtx samples.

Samples	S_{BET} (m^2/g)	V_{total} (cm^3/g)	S_{micro}[a] (m^2/g)	V_{micro}[a] (cm^3/g)
Na–Mt	55.9	0.092	3.3	0.001
TMA-$Mt_{0.25}$	69.6	0.094	19.0	0.007
TMA-$Mt_{0.5}$	147.9	0.131	59.9	0.023
TMA-$Mt_{1.0}$	154.7	0.139	61.8	0.024
TMA-$Mt_{1.5}$	173.5	0.150	65.0	0.025
TMA-$Mt_{2.0}$	160.2	0.134	55.9	0.021

[a] Microporous surface area and volume were calculated by the t-plot method.

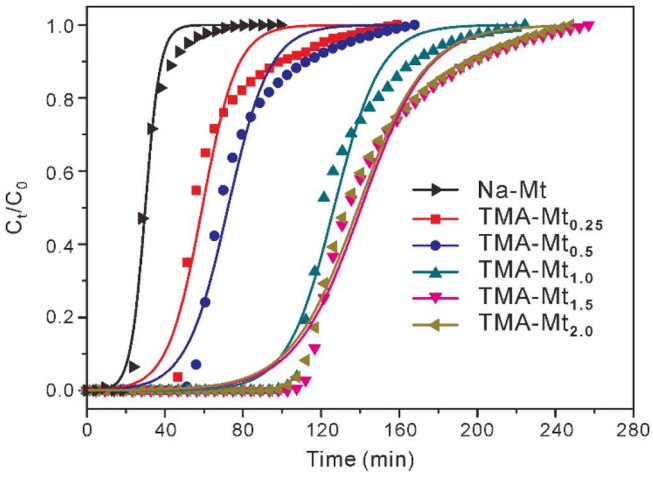

Fig. 5. Breakthrough curves of Na–Mt and TMA-Mtx samples.

Table 3
Dynamic adsorption capacity (q) and Yoon and Nelson equation parameters for benzene adsorption of Na–Mt and TMA-Mtx samples.

Samples	q (mg/g)	k	τ (min)	R^2
Na–Mt	87.1	0.263	30.0	0.990
TMA-$Mt_{0.25}$	184.3	0.113	59.1	0.972
TMA-$Mt_{0.5}$	220.9	0.094	72.3	0.982
TMA-$Mt_{1.0}$	380.8	0.083	126.6	0.986
TMA-$Mt_{1.5}$	425.3	0.059	140.6	0.985
TMA-$Mt_{2.0}$	419.0	0.058	138.9	0.987

larger than 0.34 nm) were available for benzene adsorption. Compared to Na–Mt, the q values of TMA-Mtx samples (Table 3) increased, indicating that the intercalation of TMA^+ cations enhanced the adsorption of benzene by Mt, which could be ascribed to the introduced micropores by the intercalated TMA^+ cations.

The interlayer distance of TMA-$Mt_{0.25}$ reached 0.35 nm, which was greater than the van der Waals diameter of the carbon atom (0.34 nm). As a result, a considerable number of benzene molecules could be adsorbed into the interlayer micropores of TMA-$Mt_{0.25}$, resulting in the higher q value of TMA-$Mt_{0.25}$ (184.3 mg/g) compared to that of Na–Mt (87.1 mg/g). When the dosage exceeded 0.25 CEC, the interlayer distance of TMA-Mtx samples increased to 0.41 nm, thus more micropores, which were available for benzene adsorption, were generated by the intercalated TMA^+ cations, leading to a further improvement in the benzene adsorption performance of the TMA-Mtx samples. The q value of TMA-$Mt_{1.5}$ (425.3 mg/g) was the highest among the TMA-Mtx samples because it had the largest S_{micro} (65.0 m^2/g). This result suggested that the q values of the TMA-Mtx samples correlated to their S_{micro}, confirming the significant impact of micropores on the benzene adsorption performance of TMA-Mtx samples. However, TMA-$Mt_{2.0}$ had a higher q value (419.0 mg/g) than TMA-$Mt_{0.5}$ (220.9 mg/g) and TMA-$Mt_{1.0}$ (380.8 mg/g), even though its S_{micro} (55.9 m^2/g) was smaller than those of TMA-$Mt_{0.5}$ (59.9 m^2/g) and TMA-$Mt_{1.0}$ (61.8 m^2/g). This fact indicated that interlayer micropores were not the only factor affecting the benzene adsorption performance of the TMA-Mtx samples. The superior benzene adsorption performance of TMA-$Mt_{2.0}$ towards TMA-$Mt_{0.5}$ and TMA-$Mt_{1.0}$ might be due to its larger content of TMA^+ cations (10.11%) than TMA-$Mt_{0.5}$ (5.83%) and TMA-$Mt_{1.0}$ (8.68%), as the TG curves (Fig. 3c, d, and 3f) revealed. More intercalated TMA^+ cations resulted in better hydrophobicity of the TMA-Mtx samples, improving the compatibility between TMA-Mtx and benzene molecules.

The k values of the Na–Mt and TMA-Mtx samples, which represent the diffusion and mass transfer characteristics of benzene molecules in the adsorption process, are listed in Table 3. Generally, a small k value

indicates that the adsorbate has minimal diffusion and mass transfer ability. Thus, the smaller k values of TMA-Mtx samples compared with that of Na–Mt indicated that there was lower propensity for diffusion and mass transfer of benzene molecules in TMA-Mtx samples than in Na–Mt. This may be attributable to the adsorption by the interlayer micropores introduced by intercalated TMA^+ cations. However, TMA-$Mt_{1.5}$ had a slightly larger k value (0.059) than TMA-$Mt_{2.0}$ (0.058) even though it possessed the highest S_{micro} value (65.0 m^2/g), indicating that the diffusion and mass transfer of benzene molecules occurred more easily in TMA-$Mt_{1.5}$ than in TMA-$Mt_{2.0}$. This result further confirmed that other factors aside from micropores affected the benzene adsorption of TMA-Mtx samples, which might be ascribed to the interaction between the intercalated TMA^+ cations and benzene molecules.

To detect the interaction between the benzene molecules and TMA-Mtx samples, DRIFT characterization was performed on benzene and TMA-$Mt_{1.5}$ before and after benzene adsorption. The sample obtained after TMA-$Mt_{1.5}$ adsorbed benzene was denoted TMA-$Mt_{1.5}$/Ben. The DRIFT spectra of benzene, TMA-$Mt_{1.5}$, and TMA-$Mt_{1.5}$/Ben are displayed in Fig. 6. After benzene adsorption, four bands at 3035, 3060, 3069, and 3090 cm^{-1} appeared in the DRIFT spectrum of TMA-$Mt_{1.5}$/Ben. These bands were due to the C–H stretching of aromatic rings [42–44], indicating that benzene molecules were adsorbed in TMA-$Mt_{1.5}$. In addition, these bands shifted slightly compared with those of benzene, which could be due to the interaction between adsorbed benzene molecules and intercalated TMA^+ cations. Therefore, the intercalated TMA^+ cations were also the adsorption sites for benzene molecules in addition to their introduced micropores.

Evaluation of the regeneration performance of VOCs adsorbents is an important factor for determining their industrial potential [45]. Accordingly, the breakthrough process of benzene adsorption on TMA-$Mt_{1.5}$ was performed four times (Fig. 7). The overlapping breakthrough curves of TMA-$Mt_{1.5}$ exhibited that there was good reusability of TMA-$Mt_{1.5}$ over four cycles of benzene adsorption. In addition, the recycling efficiency of TMA-$Mt_{1.5}$ after four cycles of benzene adsorption still exceeded 90% (Table 4), indicating the excellent regenerative performance of this material.

Raw minerals are potential adsorbents for VOCs treatment. Previous studies [15,46] had investigated the dynamic benzene adsorption performance of various minerals, including diatomite (Dt), kaolinite (Kaol), halloysite (Hal), calcium-based montmorillonite (Ca–Mt), and allophane (Allo). However, the microstructures and surface properties of these minerals were different with those of TMA-$Mt_{1.5}$, leading to their lower q values.

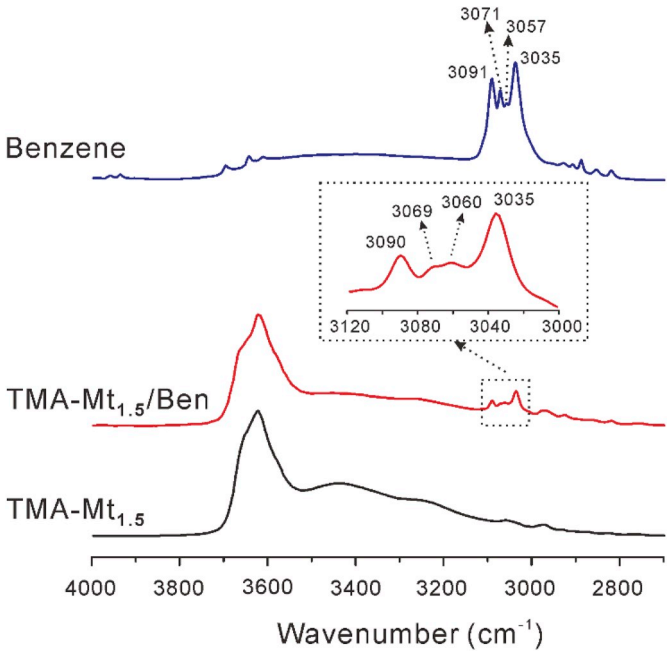

Fig. 6. DRIFT spectra of benzene, TMA-$Mt_{1.5}$, and TMA-$Mt_{1.5}$/Ben.

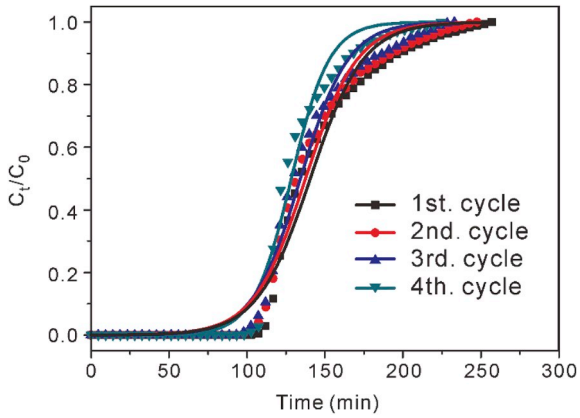

Fig. 7. Benzene adsorption breakthrough curves of TMA-$Mt_{1.5}$ cycled for four times.

Table 4
Dynamic adsorption capacity (q) and Yoon and Nelson equation parameters for various cycles of TMA-$Mt_{1.5}$.

Cycles	q (mg/g)	k	τ (min)	R^2	Efficiency (%)
First	425.3	0.059	140.6	0.985	–
Second	414.8	0.060	137.5	0.987	97.5%
Third	403.7	0.065	134.3	0.988	94.9%
Fourth	385.2	0.082	128.4	0.989	90.6%

The benzene adsorption on Dt, Kaol, and Hal mainly occurred at their surface due to the absence of appropriately sized micropores. However, their S_{BET} were relatively small, which were 17.9, 17.9, and 58.4 m^2/g, respectively, indicating the relatively small amount of surface sites for adsorption. In addition, the surfaces of Dt, Kaol, and Hal were significantly hydroxylated (and thus hydrophilic) that they were less favorable for benzene adsorption. Therefore, the q values of Dt, Kaol, and Hal, which were 74.5, 56.7, and 68.1 mg/g, respectively, were lower than that of TMA-$Mt_{1.5}$ (425.3 mg/g).

The interlayer distance of Ca–Mt (0.58 nm) was larger than that of TMA-$Mt_{1.5}$ (0.42 nm), and it was also close to the kinetic diameter of the benzene molecule (0.59 nm). Therefore, the interlayer space of Ca–Mt could theoretically accommodate benzene adsorption. However, the interlayer space of Ca–Mt was generally occupied by interlayer water, which would hinder the benzene adsorption. Therefore, the q value of Ca–Mt (141.2 mg/g) was still lower than that of TMA-$Mt_{1.5}$ (425.3 mg/g).

Allo possessed a substantial quantity of micropores, of which the S_{micro} reached 183.8 m^2/g. However, the Allo nanoparticles aggregated extensively, resulting in the formation of numerous pores with irregular channels, which are difficult for benzene molecules to penetrate. Moreover, numerous hydroxyl groups were found to be distributed on the surface of Allo. Therefore, the q value of Allo (105.9 mg/g) was lower than that of TMA-$Mt_{1.5}$ (425.3 mg/g).

Compared to activated carbon, which is flammable and generally requires high temperature steam and/or nitrogen (>120 °C) for its regeneration [47,48], TMA-$Mt_{1.5}$ can be regenerated by heating at a relatively low temperature of 120 °C after benzene adsorption. Moreover, TMA-$Mt_{1.5}$ has a high recycling efficiency (exceeded 90%) after four cycles of benzene adsorption. Therefore, TMA-$Mt_{1.5}$ appears to have a greater thermal regeneration advantage than activated carbon.

4. Conclusion

In this study, the roles of TMA^+ cations in the microstructure and dynamic benzene adsorption performance of TMA-Mts with various TMA^+ dosages were investigated. TMA^+ was intercalated into the interlayer space of Mt, with the numbers of micropores generated depending on the dosage of TMA^+.

The microporous surface area increased with the increase of TMA^+ dosage, and achieved a maximum at 1.5 CEC. The addition of more TMA^+ cations (e.g., >2.0 CEC) led to a decline of microporous surface area due to the closer packing of TMA^+ cations. The dynamic benzene adsorption capacity of TMA-Mts was positively influenced by their microporous surface area.

In addition to micropores, the intercalated TMA^+ cations were another site for benzene adsorption, enhancing the benzene adsorption performance of TMA-Mts but decreasing the diffusion and mass transfer of benzene molecules through TMA-Mts. It has thus been shown that TMA-Mt may be utilized as an effective VOCs adsorbent due to its excellent dynamic benzene adsorption performance and superior regenerability.

Declaration of competing interests

We declare that we have no known competing financial interests or personal relationships that could have appeared to influence the work reported in this paper.

CRediT authorship contribution statement

Liangliang Deng: Conceptualization, Investigation, Writing - original draft. **Yaqi Liu:** Investigation. **Guanzheng Zhuang:** Writing - review & editing. **Peng Yuan:** Supervision. **Dong Liu:** Resources. **Hongling Bu:** Resources. **Hongzhe Song:** Resources. **Li Li:** Resources.

Acknowledgements

Financial supports from the Science and Technology Planning Project of Guangdong Province, China (Grant No. 2017B020237003) and National Natural Science Foundation of China (Grant No. 41672042) and Youth Innovation Promotion Association of CAS for the excellent members (2016-81-01) and Natural Science Foundation for Distinguished Young Scientists of Guangdong Province (Grant No. 2016A030306034) and the Youth Top-notch Talent Special Support Program of Guangdong Province (Grant No. 609254605090) are gratefully acknowledged. This is a contribution No. IS-2798 from GIGCAS.

References

[1] P. Wang, W. Zhao, Assessment of ambient volatile organic compounds (VOCs) near major roads in urban Nanjing, China, Atmos. Res. 89 (2008) 289–297.
[2] Z.H. Ling, H. Guo, Contribution of VOC sources to photochemical ozone formation and its control policy implication in Hong Kong, Environ. Sci. Policy 38 (2014) 180–191.
[3] M. Claeys, W. Wang, A.C. Ion, I. Kourtchev, A. Gelencsér, W. Maenhaut, Formation of secondary organic aerosols from isoprene and its gas-phase oxidation products through reaction with hydrogen peroxide, Atmos. Environ. 38 (2004) 4093–4098.
[4] D. Melanie, K.G. Sexton, J. Harvey, B. Kevin, J. Ilona, Effects of 1,3-butadiene, isoprene, and their photochemical degradation products on human lung cells, Environ. Health Perspect. 112 (2004) 1488–1495.
[5] Y. Liu, X. Feng, D. Lawless, Separation of gasoline vapor from nitrogen by hollow fiber composite membranes for VOC emission control, J. Membr. Sci. 271 (2006) 114–124.
[6] J. Luo, Q. Zhang, A. Huang, S.L. Suib, Total oxidation of volatile organic compounds with hydrophobic cryptomelane-type octahedral molecular sieves, Microporous Mesoporous Mater. 35 (2000) 209–217.
[7] S. Zuo, R. Zhou, Influence of synthesis condition on pore structure of Al pillared clays and supported Pd catalysts for deep oxidation of benzene, Microporous Mesoporous Mater. 113 (2008) 472–480.
[8] B. Guieysse, C. Hort, V. Platel, R. Munoz, M. Ondarts, S. Revah, Biological treatment of indoor air for VOC removal: potential and challenges, Biotechnol. Adv. 26 (2008) 398–410.
[9] W. Yuan, Y. Peng, L. Dong, W. Yu, L. Deng, F. Chen, Novel hierarchically porous nanocomposites of diatomite-based ceramic monoliths coated with silicalite-1 nanoparticles for benzene adsorption, Microporous Mesoporous Mater. 206 (2015) 184–193.
[10] W. Yu, L. Deng, P. Yuan, D. Liu, W. Yuan, F. Chen, Preparation of hierarchically porous diatomite/MFI-type zeolite composites and their performance for benzene adsorption: the effects of desilication, Chem. Eng. J. 270 (2015) 450–458.
[11] D. Liu, P. Yuan, D. Tan, H. Liu, T. Wang, M. Fan, J. Zhu, H. He, Facile preparation of hierarchically porous carbon using diatomite as both template and catalyst and methylene blue adsorption of carbon products, J. Colloid Interface Sci. 388 (2012) 176–184.
[12] Z. Li, Y. Liu, X. Yang, Y. Xing, Q. Yang, R.T. Yang, Adsorption thermodynamics and desorption properties of gaseous polycyclic aromatic hydrocarbons on mesoporous adsorbents, Adsorption 23 (2017) 361–371.
[13] W. Song, R. Justice, C. Jones, V. Grassian, S. Larsen, Synthesis, characterization, and adsorption properties of nanocrystalline ZSM-5, Langmuir 20 (2004) 8301–8306.
[14] J. Pires, A. Carvalho, M.B. de Carvalho, Adsorption of volatile organic compounds in Y zeolites and pillared clays, Microporous Mesoporous Mater. 43 (2001) 277–287.
[15] L. Deng, P. Yuan, D. Liu, F. Annabi-Bergaya, J. Zhou, F. Chen, Z. Liu, Effects of microstructure of clay minerals, montmorillonite, kaolinite and halloysite, on their benzene adsorption behaviors, Appl. Clay Sci. 143 (2017) 184–191.
[16] C. Almeida, N. Debacher, A. Downs, L. Cottet, C. Mello, Removal of methylene blue from colored effluents by adsorption on montmorillonite clay, J. Colloid Interface Sci. 332 (2009) 46–53.
[17] O. Abollino, M. Aceto, M. Malandrino, C. Sarzanini, E. Mentasti, Adsorption of heavy metals on Na-montmorillonite. Effect of pH and organic substances, Water Res. 37 (2003) 1619–1627.
[18] X. Liu, R. Zhu, J. Ma, F. Ge, Y. Xu, Y. Liu, Molecular dynamics simulation study of benzene adsorption to montmorillonite: influence of the hydration status, Colloids Surf., A 434 (2013) 200–206.
[19] L. Ma, Q. Chen, J. Zhu, Y. Xi, H. He, R. Zhu, Q. Tao, G.A. Ayoko, Adsorption of phenol and Cu (II) onto cationic and zwitterionic surfactant modified montmorillonite in single and binary systems, Chem. Eng. J. 283 (2016) 880–888.
[20] Y. Xi, Q. Zhou, R.L. Frost, H. He, Thermal stability of octadecyltrimethylammonium bromide modified montmorillonite organoclay, J. Colloid Interface Sci. 311 (2007) 347–353.
[21] B. Hu, H. Luo, Adsorption of hexavalent chromium onto montmorillonite modified with hydroxyaluminum and cetyltrimethylammonium bromide, Appl. Surf. Sci. 257 (2010) 769–775.
[22] J. Pan, G. Yang, B. Han, H. Yan, Studies on interaction of dodecyltrimethylammonium bromide with Na-and Al-montmorillonite, J. Colloid Interface Sci. 194 (1997) 276–280.
[23] J.J. Stevens, S.J. Anderson, S.A. Boyd, FTIR study of competitive water-arene sorption on tetramethylammonium-and trimethylphenylammonium-montmorillonites, Clay Clay Miner. 44 (1996) 88–95.
[24] N. Liu, M.-x. Wang, M.-m. Liu, F. Liu, L. Weng, L.K. Koopal, W.-f. Tan, Sorption of tetracycline on organo-montmorillonites, J. Hazard Mater. 225 (2012) 28–35.
[25] Y. Park, Z. Sun, G.A. Ayoko, R.L. Frost, Bisphenol A sorption by organo-montmorillonite: implications for the removal of organic contaminants from water, Chemosphere 107 (2014) 249–256.
[26] H. Zhao, G.F. Vance, Sorption of trichloroethylene by organo-clays in the presence of humic substances, Water Res. 32 (1998) 3710–3716.
[27] S. Lin, M. Cheng, Adsorption of phenol and m-chlorophenol on organobentonites and repeated thermal regeneration, Waste Manag. 22 (2002) 595–603.
[28] L. Zhu, B. Chen, X. Shen, Sorption of phenol, p-nitrophenol, and aniline to dual-cation organobentonites from water, Environ. Sci. Technol. 34 (2000) 468–475.
[29] C.-C. Wang, L.-C. Juang, C.-K. Lee, T.-C. Hsu, J.-F. Lee, H.-P. Chao, Effects of exchanged surfactant cations on the pore structure and adsorption characteristics of montmorillonite, J. Colloid Interface Sci. 280 (2004) 27–35.
[30] C. Long, Y. Li, W. Yu, A. Li, Removal of benzene and methyl ethyl ketone vapor: comparison of hypercrosslinked polymeric adsorbent with activated carbon, J. Hazard Mater. 203 (2012) 251–256.
[31] R.K. Kukkadapu, S.A. Boyd, Tetramethylphosphonium-and tetramethylammonium-smectites as adsorbents of aromatic and chlorinated hydrocarbons: effect of water on adsorption efficiency, Clay Clay Miner. 43 (1995) 318–323.
[32] J.-F. Lee, M.M. Mortland, C.T. Chiou, D.E. Kile, S.A. Boyd, Adsorption of benzene, toluene, and xylene by two tetramethylammonium-smectites having different charge densities, Clay Clay Miner. 38 (1990) 113–120.
[33] G. Wang, B. Dou, Z. Zhang, J. Wang, H. Liu, Z. Hao, Adsorption of benzene, cyclohexane and hexane on ordered mesoporous carbon, J. Environ. Sci. 30 (2015) 65–73.
[34] L. Zhu, R. Zhu, L. Xu, X. Ruan, Influence of clay charge densities and surfactant loading amount on the microstructure of CTMA–montmorillonite hybrids, Colloids Surf., A 304 (2007) 41–48.
[35] S. Brunauer, P.H. Emmett, E. Teller, Adsorption of gases in multimolecular layers, J. Am. Chem. Soc. 60 (1938) 309–319.
[36] B.C. Lippens, J. De Boer, Studies on pore systems in catalysts: V. The t method, J. Catal. 4 (1965) 319–323.
[37] M. Thommes, K. Kaneko, A.V. Neimark, J.P. Olivier, F. Rodriguez-Reinoso, J. Rouquerol, K.S. Sing, Physisorption of gases, with special reference to the

evaluation of surface area and pore size distribution (IUPAC Technical Report), Pure Appl. Chem. 87 (2015) 1051–1069.
[38] Y.H. Yoon, J.H. Nelson, Application of gas adsorption kinetics I. A theoretical model for respirator cartridge service life, Am. Ind. Hyg. Assoc. J. 45 (1984) 509–516.
[39] G. Zhuang, Z. Zhang, J. Sun, L. Liao, The structure and rheology of organo-montmorillonite in oil-based system aged under different temperature, Appl. Clay Sci. 124 (2016) 21–30.
[40] J. Zhu, W. Shen, Y. Ma, L. Ma, Q. Zhou, P. Yuan, D. Liu, H. He, The influence of alkyl chain length on surfactant distribution within organo-montmorillonites and their thermal stability, J. Therm. Anal. Calorim. 109 (2012) 301–309.
[41] Y. Wang, P. Zhang, K. Wen, X. Su, J. Zhu, H. He, A new insight into the compositional and structural control of porous clay heterostructures from the perspective of NMR and TEM, Microporous Mesoporous Mater. 224 (2016) 285–293.
[42] A. Palazov, Benzene adsorption and its interaction with carbon monoxide on alumina-supported platinum—an infrared spectroscopic study, J. Catal. 30 (1973) 13–20.
[43] A. De Mallmann, D. Barthomeuf, Change in benzene adsorption with acidobasicity of (Cs, Na) X zeolites studied by ir spectroscopy, Zeolites 8 (1988) 292–301.
[44] Y. Du, H. Wang, S. Chen, Study on alkylation of benzene with ethylene over β-zeolite catalyst to ethylbenzene by in situ IR, J. Mol. Catal. A Chem. 179 (2002) 253–261.
[45] W. Wang, X. Ma, S. Grimes, H. Cai, M. Zhang, Study on the absorbability, regeneration characteristics and thermal stability of ionic liquids for VOCs removal, Chem. Eng. J. 328 (2017) 353–359.
[46] L. Deng, P. Du, W. Yu, P. Yuan, F. Annabi-Bergaya, D. Liu, J. Zhou, Novel hierarchically porous allophane/diatomite nanocomposite for benzene adsorption, Appl. Clay Sci. 168 (2019) 155–163.
[47] E. Sabio, E. González, J. González, C. González-García, A. Ramiro, J. Ganan, Thermal regeneration of activated carbon saturated with p-nitrophenol, Carbon 42 (2004) 2285–2293.
[48] K.S. Hwang, D.K. Choi, S.Y. Gong, S.Y. Cho, Adsorption and thermal regeneration of methylene chloride vapor on an activated carbon bed, Chem. Eng. Sci. 52 (1997) 1111–1123.